

Sub-Diffraction-Limit Imaging System with two Interfacing Hyperbolic Metamaterials

Kirill Bronnikov^{1,2}, Jesús Arriaga,³ Arkadii Krokhin^{1,4,*} and Vladimir P. Drachev^{1,4,†}

¹*Skolkovo Institute of Science and Technology, Russian Federation, Moscow 143025, Russia*

²*Institute of Automation and Electrometry of the SB RAS, Russian Federation, Novosibirsk 630090, Russia*

³*Instituto de Física, Universidad Autónoma de Puebla, Apartado Postal J-48, Puebla 72570, Mexico*

⁴*Department of Physics, University of North Texas, 1155 Union Circle #311427, Denton, Texas 76203, USA*



(Received 5 May 2021; revised 24 August 2021; accepted 30 September 2021; published 27 October 2021)

It is demonstrated that a system of two interfacing hyperbolic metamaterials may be used for direct subwavelength imaging in the visible range. The proposed configuration consists of two anisotropic photonic crystals: a multilayered metal-dielectric structure and an adjoined wired structure. The results of analytical calculations and numerical modeling show that the light emitted by a dipole placed on the top of the multilayered structure propagates within a narrow cone along the direction \mathbf{n} , where $\text{Re } \epsilon(\omega, \mathbf{n}) = 0$. Owing to impedance matching and negative refraction at the interface, a bright image with a maximum transverse size of approximately 50 nm is focused in the wired structure at the wavelength $\lambda = 670$ nm.

DOI: 10.1103/PhysRevApplied.16.044054

I. INTRODUCTION

A perfect flat lens proposed by Veselago [1] and mathematically justified by Pendry [2] consists of a slab of metamaterial with $n = -1$ surrounded by a medium with $n = 1$. It can produce an ideal image because it collects all propagating and evanescent waves emitted by a source and transfers them to the image without losses due to perfectly matching layers. Dispersion and absorption in real materials place a natural limit for the resolution [3] that makes the concept of a perfect lens flawed. Nevertheless, a negative refractive index slab serves as a flat superlens breaking the subwavelength limit in optics [4–6]. Recently, a Veselago flat lens was experimentally realized in the microwave region [7], where a negative refractive index $n = -1$ was obtained with a slab of Weyl metacrystal.

Imaging in the far-field with subwavelength resolution requires transformation of evanescent modes radiated by an object in the near-field to propagating waves. This transformation was achieved by introducing a multilayered cylindrical [8–10] or spherical [11] stack of hyperbolic metamaterial (HMM) into a projecting device. Application of HMM in optical devices allows the realization of subwavelength interference pattern from multilayered slab [12] or array of metallic nanowires in dielectric [13]. Although these studies demonstrate a possibility of manipulating with light patterns at subwavelength scales, they do not consider a question about imaging of an object

at the focal plane. Two-slit interference was applied for subwavelength photolithography for gratings fabrication [12]. Here we propose a structure of two planar HMMs that allows subwavelength imaging of a light source. This focusing system allows photolithography of any image produced in the focus plane. Owing to hyperbolic dispersion, the emitted light propagates in each HMM along narrow epsilon-near-zero channels, suffering from negative refraction at the interface. However, the effects of dispersion and dissipation in the metallic constituents of the structure are explicitly taken into account. The parameters of the HMMs media are selected to satisfy the matching of impedances at the interface that strongly reduces losses at reflection. As a result, the record-high transmission is numerically achieved for silver-aluminum and silver-silica constituents allowing bright images with subwavelength resolution exceeding the values reported in the modern literature. Specifically, we obtain the focal spot size to wavelength ratio $l/\lambda = 0.075$ versus the values 0.41 and 0.37 reported in Refs. [10,11] respectively.

II. IMAGING SYSTEM DESIGN

There are two types of hyperbolic media within the class of uniaxial optical crystals. For type I the isofrequency surfaces are two-sheet hyperboloids, and for type II they are one-sheet hyperboloids, shown schematically in Fig. 1. The optical axis is along axis z with the corresponding component of permittivity tensor $\epsilon_z = \epsilon_{\parallel}$. In the x - y plane the crystal is isotropic with $\epsilon_x = \epsilon_y = \epsilon_{\perp}$.

*arkady@unt.edu

†v.drachev@skoltech.ru

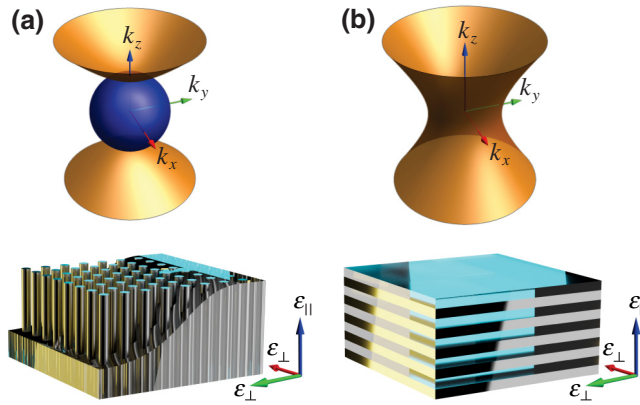


FIG. 1. Two isofrequency surfaces of an extraordinary wave with hyperbolic dispersion. (a) Hyperboloid of two sheets corresponding to type I HMM. It can be realized as a photonic crystal of metallic rods in dielectric matrix. The blue sphere is an isofrequency surface of an ordinary wave. (b) Hyperboloid of one sheet corresponding to type II HMM. Can be realized as a superlattice of metal and dielectric layers.

In type I HMM, the metallic properties dominate along axis z , therefore $\varepsilon_{\parallel} < 0$ and $\varepsilon_{\perp} > 0$. The dispersion of the extraordinary wave is given by

$$\frac{k_x^2 + k_y^2}{|\varepsilon_{\parallel}|} - \frac{k_z^2}{\varepsilon_{\perp}} = -\frac{\omega^2}{c^2}. \quad (1)$$

In type II HMM, metal conductivity dominates in the x - y plane, i.e., $\varepsilon_{\parallel} > 0$ and $\varepsilon_{\perp} < 0$. The dispersion relation for extraordinary wave is

$$\frac{k_x^2 + k_y^2}{\varepsilon_{\parallel}} - \frac{k_z^2}{|\varepsilon_{\perp}|} = \frac{\omega^2}{c^2}. \quad (2)$$

The ordinary wave propagates in a uniaxial crystal as in an isotropic medium with refractive index $\sqrt{|\varepsilon_{\perp}|}$.

Let us consider the refraction of an extraordinary plane wave at the horizontal interface $z = 0$ between two hyperbolic media. Let the region $z > 0$ be filled by type II HMM with $\varepsilon_{\parallel} = 3.9$ and $\varepsilon_{\perp} = -7$ and the lower semispace $z < 0$ be filled by type I HMM with $\varepsilon_{\parallel} = -3.9$ and $\varepsilon_{\perp} = 7$. The dielectric properties of the upper and lower media are mutually “conjugated” in order to minimize the reflection losses, as shown in the following.

The dispersion relations for these HMMs are given in Fig. 2 by red (HMM II) and blue (HMM I) hyperbolas. The wave vector \mathbf{k}_i in the incoming wave has components ($k_{x(i)} > 0$, $k_{z(i)} > 0$). For this wave vector, the group velocity $\mathbf{v}_{g(i)} = \nabla\omega(\mathbf{k})|_{\mathbf{k}=\mathbf{k}_i}$ has a negative vertical projection that corresponds to energy propagation towards the interface. Although the vertical component of \mathbf{k}_i is positive, i.e., the phase grows outward of the interface, this wave transfers energy from the upper to lower semispace.

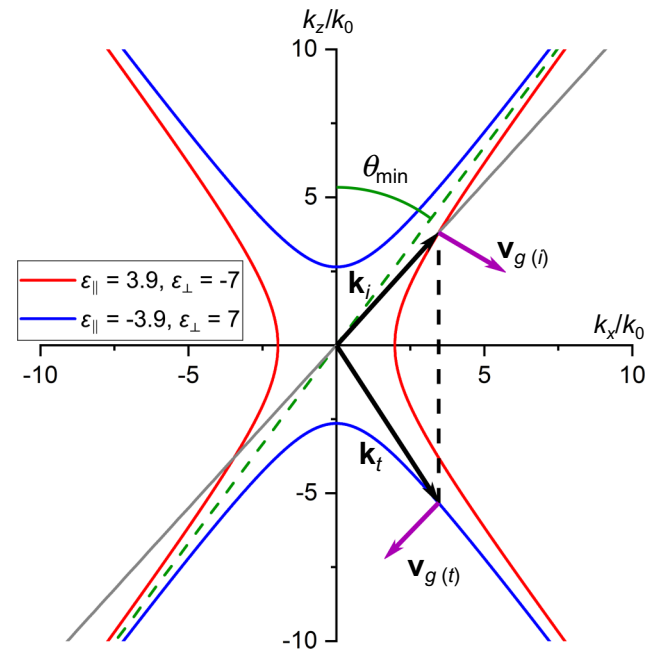


FIG. 2. Scheme of negative refraction at the interface between two hyperbolic media. The incident plane wave, characterized by wave vector \mathbf{k}_i and group velocity $\mathbf{v}_{g(i)}$, comes from type II HMM ($z > 0$) with $\varepsilon_{\parallel} = 3.9$, $\varepsilon_{\perp} = -7$. The red hyperbola shows dispersion in this medium given by Eq. (2), where $k_0 = \omega/c$. After negative refraction at the interface $z = 0$, the plane wave is transmitted to type I HMM ($z < 0$) with $\varepsilon_{\parallel} = -3.9$, $\varepsilon_{\perp} = 7$ with dispersion shown by the blue hyperbola, Eq. (1). The transmitted wave has the wave vector \mathbf{k}_t and group velocity $\mathbf{v}_{g(t)}$.

A backward propagation regime is typical for waves in HMMs when phase and group velocities have opposite projections [14].

The wave vector \mathbf{k}_t of the transmitted wave is obtained from the momentum conservation, $k_{x(i)} = k_{x(t)}$. From two points on the blue hyperbola, satisfying this conservation law, the point on the low branch corresponds to the refracted wave, because here the vertical projection of group velocity is negative.

Mutual orientation of the vectors of group velocities in the incident and refracted wave in Fig. 2 is a signature of negative refraction at the interface between two HMMs of different types. Here we show that due to negative refraction at the interface between two weakly absorbing HMMs, a real subwavelength image is formed by converging rays, similarly to an image obtained with an ideal Pendry’s flat lens.

It follows from the plot in Fig. 2 that the incoming wave is a propagating mode if the angle of incidence θ exceeds the critical value $\theta_{\min} = \arctan \sqrt{|\varepsilon_{\parallel}/\varepsilon_{\perp}|} = \arctan(\sqrt{3.9/7})$. Here the angle θ_{\min} defines the hyperbola’s asymptote $k_z = \sqrt{|\varepsilon_{\perp}/\varepsilon_{\parallel}|} k_x$.

We briefly remind the fundamental properties of monochromatic plane wave propagating in a medium with

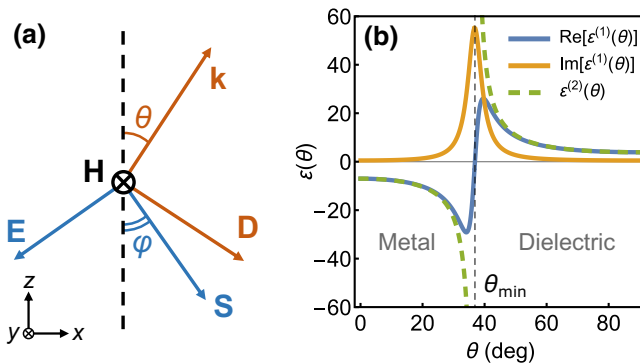


FIG. 3. (a) Mutual orientation of the vectors in a plane wave propagating in a uniaxial crystal with optical axis along the dashed line. Pairs of orthogonal vectors are marked by the same color. The direction of Poynting's vector \mathbf{S} corresponds to a medium with hyperbolic dispersion, as it follows from the direction of group velocity $\mathbf{v}_{g(i)}$ in Fig. 2. Angles θ and φ are related, $\tan \varphi = \text{Re} \left(\frac{\epsilon_{\perp}}{\epsilon_{\parallel}} \right) \tan \theta$ [15]. (b) Angular dependence of the dielectric permittivity in a dissipative hyperbolic medium with $\epsilon_{\perp}^{(1)} = -7 + i 0.5$, $\epsilon_{\parallel}^{(1)} = 3.9 + i 0.5$ and in a dissipationless hyperbolic medium with $\epsilon_{\perp}^{(2)} = -7$, $\epsilon_{\parallel}^{(2)} = 3.9$.

uniaxial anisotropy and hyperbolic dispersion. It follows from Maxwell's equations

$$(\omega/c)\mathbf{H} = \mathbf{k} \times \mathbf{E}, \quad (\omega/c)\mathbf{D} = -\mathbf{k} \times \mathbf{H} \quad (3)$$

that the mutual orientation of the vectors \mathbf{k} , E , D , H , and the Pointing vector $\mathbf{S} = (c/4\pi)(\mathbf{E} \times \mathbf{H})$ is as shown in Fig. 3(a). The four vectors, \mathbf{k} , E , D , S are coplanar because each of them is orthogonal to \mathbf{H} . The optical axis also lies in the same plane. The direction of propagation of electromagnetic energy is defined by the vector of group velocity $\mathbf{v}_g = \partial \omega(\mathbf{k})/\partial \mathbf{k}$, which coincides with the direction of the Pointing's vector \mathbf{S} for a transparent (or weakly absorbing) media.

For the extraordinary wave, the length of the wave vector $k = (\omega/c)\sqrt{\epsilon(\theta)}$ depends on the angle θ it makes with the optical axis, where the angular dependence of the dielectric constant is given by the equation [15]

$$\frac{1}{\epsilon(\theta)} = \frac{\sin^2 \theta}{\epsilon_{\parallel}} + \frac{\cos^2 \theta}{\epsilon_{\perp}}. \quad (4)$$

In a dissipationless type II HMM ($\epsilon_{\parallel} > 0$, $\epsilon_{\perp} < 0$) the dependence $\epsilon(\theta)$ has a point of singularity at $\theta = \theta_{\min}$ where $\epsilon(\theta_{\min}) = \infty$. At this point the function $\epsilon(\theta)$ changes its sign suffering from an infinite discontinuity, see the green line in Fig. 3(b). Dissipation removes this singularity. The real part of $\epsilon(\theta)$ changes its sign passing through zero, as shown by the blue line. In this case, the angle θ_{\min} obtained from the equation $\text{Re } \epsilon(\theta) = 0$ is shifted by $-(\delta^2/2)(\epsilon_{\parallel} - |\epsilon_{\perp}|/(\epsilon_{\parallel}|\epsilon_{\perp}|)^{3/2})$ from the angle $\arctan(\sqrt{\epsilon_{\parallel}/|\epsilon_{\perp}|})$, where $\delta = \text{Im } \epsilon_{\perp} = \text{Im } \epsilon_{\parallel}$.

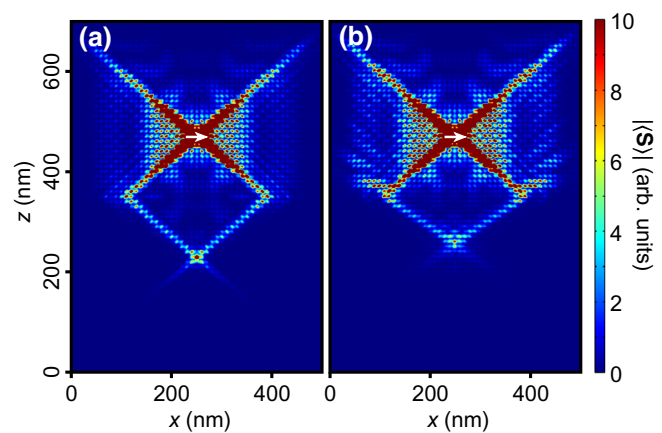


FIG. 4. Near-field subwavelength image of a point dipole (shown by white arrow) with $\lambda = 670$ nm obtained by negative refraction at the interface between two HMMs. Color map shows spatial distribution of Poynting's vector. (a) The HMMs satisfy the condition (9) of minimum reflection: $\epsilon_{\parallel}^a = 3.9$, $\epsilon_{\perp}^a = -7 + 0.18i$, $\epsilon_{\parallel}^b = -3.9 + 0.18i$, and $\epsilon_{\perp}^b = 7 + 0.26i$. (b) Less dissipative HMMs with parameters not matching the condition of minimum reflection: $\epsilon_{\parallel}^a = 4$, $\epsilon_{\perp}^a = -7 + 0.1i$, $\epsilon_{\parallel}^b = -2 + 0.1i$, and $\epsilon_{\perp}^b = 9 + 0.1i$.

The line $\theta = \theta_{\min}$ divides space into two parts with metallic ($\text{Re } \epsilon(\theta) < 0$) and dielectric ($\text{Re } \epsilon(\theta) > 0$) response. It is known that the surface plasmon-polariton is an eigenmode propagating along the metal-dielectric interface [15]. As the virtual boundary $\theta = \theta_{\min}$ separates the metal region from the dielectric region, a bulk plasmon-polariton mode may propagate along it [16,17]. This mode is tightly localized and it serves as a carrier of the subwavelength image.

III. SUBWAVELENGTH IMAGE OBTAINED FOR TWO HOMOGENEOUS HYPERBOLIC MEDIA

Let us consider two semi-infinite, homogeneous, hyperbolic media with interface at $z = 0$. The upper medium (a) is the type II HMM with $\text{Re } \epsilon_{\parallel}^a > 0$, $\text{Re } \epsilon_{\perp}^a < 0$. The lower medium (b) is the type I HMM with $\text{Re } \epsilon_{\parallel}^b < 0$, $\text{Re } \epsilon_{\perp}^b > 0$. The optical axis in each medium coincides with axis z . The light source is a point dipole oriented perpendicular to axis z placed in the upper medium at 120 nm above the interface, as shown in Fig. 4. The dipole radiates at the wavelength $\lambda = 670$ nm. Its image with subwavelength resolution is formed in the near-field zone.

The parameters of the hyperbolic media must be optimized to minimize reflection losses for the extraordinary (TM) wave. Although the field emitted by the dipole also contains the TE mode (with electric field parallel to the interface), it does not propagate in the upper medium where $\epsilon_{\perp}^a < 0$. The fields of the incident TM wave propagating in the upper medium are oriented as shown in Fig. 3(a). The fields of the reflected wave and refracted wave

are calculated from the electrodynamics boundary conditions. The details of calculation are given in the [Appendix](#). The following formula gives the reflection coefficient defined as $R = |H_r|^2/|H_i|^2$:

$$R(\theta) = \left| \frac{\cos \theta \sqrt{\varepsilon_{\perp}^b \varepsilon^a(\theta)} + \varepsilon_{\perp}^a \sqrt{1 - \frac{\varepsilon^a(\theta)}{\varepsilon_{\parallel}^b} \sin^2 \theta}}{\cos \theta \sqrt{\varepsilon_{\perp}^b \varepsilon^a(\theta)} - \varepsilon_{\perp}^a \sqrt{1 - \frac{\varepsilon^a(\theta)}{\varepsilon_{\parallel}^b} \sin^2 \theta}} \right|^2. \quad (5)$$

Here $\varepsilon^a(\theta) = \varepsilon_{\parallel}^a |\varepsilon_{\perp}^a| / (|\varepsilon_{\perp}^a| \sin^2 \theta - \varepsilon_{\parallel}^a \cos^2 \theta)$ is the angular dependence of permittivity in medium a given by Eq. (4). Note that for $\theta > \theta_{\min}$ the function $\varepsilon^a(\theta)$ takes only positive values.

The condition of total transmission, $R(\theta) = 0$, is satisfied if

$$\cos \theta \sqrt{\varepsilon_{\perp}^b \varepsilon^a(\theta)} + \varepsilon_{\perp}^a \sqrt{1 - \frac{\varepsilon^a(\theta)}{\varepsilon_{\parallel}^b} \sin^2 \theta} = 0. \quad (6)$$

If the dielectric constants of both hyperbolic media are real, this equation has the root

$$\theta_B = \arctan \left(\frac{\varepsilon_{\parallel}^a |\varepsilon_{\parallel}^b|}{|\varepsilon_{\perp}^a|^2} \cdot \frac{|\varepsilon_{\perp}^a| + \varepsilon_{\perp}^b}{\varepsilon_{\parallel}^a + |\varepsilon_{\parallel}^b|} \right)^{1/2}, \quad (7)$$

which is the Brewster angle for the interface between two uniaxial media. Note that the angle θ defines the direction of the wave vector \mathbf{k} , which is different from the direction of Poynting vector \mathbf{S} , see Fig. 3. For two isotropic media with linear dispersion Eq. (7) is reduced to the well-known result, $\theta_B = \arctan(\sqrt{\varepsilon^b/\varepsilon^a})$.

If the light source is placed in the upper medium (medium (a) in Fig. 4) the emitted radiation propagates within a narrow cone [20] along the line φ_0 defined from $\tan \varphi_0 = (|\varepsilon_{\perp}^a|/\varepsilon_{\parallel}^a) \tan \theta_{\min}$, see Fig. 3. Thus, to realize the condition of minimum reflection, the angle of incidence θ_{\min} must be the Brewster angle: $\theta_B = \theta_{\min}$. This occurs for symmetrically conjugated media, when $\varepsilon_{\parallel}^a = |\varepsilon_{\parallel}^b|$ and $|\varepsilon_{\perp}^a| = \varepsilon_{\perp}^b$. As the function $\varepsilon^a(\theta) \rightarrow \infty$ at $\theta \rightarrow \theta_{\min}$, the value of the reflection coefficient is calculated by L'Hôpital's rule that gives $\lim R(\theta)_{\theta \rightarrow \theta_{\min}} = 0$. According to Fig. 2, in a nondissipative hyperbolic medium the wave incident at $\theta = \theta_{\min}$ has $k_z \rightarrow \infty$. This means that total transmission cannot be realized at $\theta = \theta_{\min}$. However, almost total transmission occurs for the angle slightly exceeding θ_{\min} and finite wave vector, if the media are dissipative. Angular dependence of the reflection coefficient (5) is shown in Fig. 5 for dissipationless (green line), weakly dissipative (blue line), and moderately dissipative (yellow line) structures. Even in the latter case the reflection remains very weak near $\theta_{\min} = \arctan \sqrt{3.9/7} \approx 0.641 \approx 36.74^\circ$ and the minimum is slightly shifted towards larger angles.

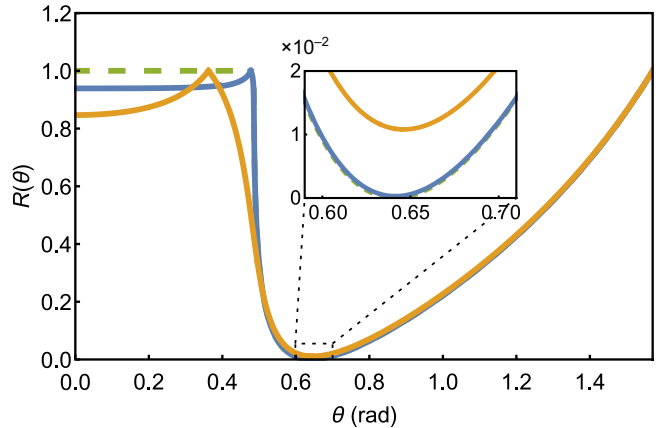


FIG. 5. Reflection coefficient versus angle of incidence. The green line is for nondissipative media: $\varepsilon_{\parallel}^a = 3.9$, $\varepsilon_{\perp}^a = -7$, $\varepsilon_{\parallel}^b = -3.9$, and $\varepsilon_{\perp}^b = 7$. The blue line is for weakly dissipative media: $\varepsilon_{\parallel}^a = 3.9$, $\varepsilon_{\perp}^a = -7 + 0.18i$, $\varepsilon_{\parallel}^b = -3.9 + 0.18i$, and $\varepsilon_{\perp}^b = 7 + 0.26i$. The yellow line is for moderately dissipative media: $\varepsilon_{\parallel}^a = 3.9 + 0.5i$, $\varepsilon_{\perp}^a = -7 + 0.7i$, $\varepsilon_{\parallel}^b = -3.9 + 0.2i$, and $\varepsilon_{\perp}^b = 7 + 0.3i$. An enlarged view of the region near the minimum is shown in the inset.

The interface between two hyperbolic dissipationless media remains perfectly reflective for the angles of incidence $0 \leq \theta \leq \theta_c$, where

$$\theta_c = \arctan \sqrt{\frac{\varepsilon_{\parallel}^a |\varepsilon_{\parallel}^b|}{|\varepsilon_{\perp}^a| (\varepsilon_{\parallel}^a + |\varepsilon_{\parallel}^b|)}} \quad (8)$$

is the root of the equation $\varepsilon_{\parallel}^b = \varepsilon^a(\theta) \sin^2 \theta$. For the selected parameters of the media the critical angle is $\theta_c = \arctan \sqrt{3.9/14} \approx 0.486 \approx 27.83^\circ$. It is shown in the [Appendix](#) that at $\theta = \theta_c$ the z -component of \mathbf{k} , vanishes. For $\theta \leq \theta_c$ the wave vector in medium (b) becomes pure imaginary. As $\theta_c < \theta_{\min}$, the wave vector for the wave incident at angle θ_c is also pure imaginary. Thus, an interesting optical phenomenon, total internal reflection of an evanescent wave at the interface between two hyperbolic media, occurs for $\theta_c < \theta_{\min}$. This is the reason for $R = 1$ at $\theta < \theta_c$ for the green dashed curve in Fig. 5. The dependence $R(\theta)$ exhibits a singularity, at $\theta = \theta_c$, which is related to vanishing Poynting vectors in both media when $\theta \rightarrow \theta_c$.

At $\theta > \theta_c$ the z -component of transmitted wave becomes real, giving rise to a sharply increasing transmission, which becomes perfect ($R = 0$) at $\theta = \theta_{\min}$ due to excitation of bulk plasmon-polariton. For larger angles, $\theta > \theta_{\min}$, both media exhibit a dielectric behavior and the reflection coefficient growth, approaching 1 for $\theta = \pi/2$. Note that for two hyperbolic media the effect of total internal reflection takes place for small angles of incidence, unlike the same effect in dielectrics, where the angle of incidence must exceed some critical value. If both media

are isotropic, Eq. (8) for θ_c is reduced to the well-known result $\theta_c = \arcsin \sqrt{\varepsilon^b / \varepsilon^a}$.

Finite dissipation smoothes the singularity of $R(\theta)$ at $\theta = \theta_c$ but the behavior of this function remain practically the same, as can be seen from the plots in Fig. 5. The minimum of reflection occurs very close to the angle $\theta = \theta_{\min}$ for dissipative HMMs with conjugated parameters:

$$|\operatorname{Re} \varepsilon_{\perp}^a| = \operatorname{Re} \varepsilon_{\perp}^b, \quad \operatorname{Re} \varepsilon_{\parallel}^a = |\operatorname{Re} \varepsilon_{\parallel}^b|. \quad (9)$$

This condition is satisfied for the imaging system shown in Fig. 4(a) and it is broken for the system in Fig. 4(b). Both figures demonstrate the distribution of Poynting's vector \mathbf{S} of a point dipole radiation obtained by COMSOL MULTIPHYSICS. Although the structure in Fig. 4(a) is more dissipative, it produces a brighter image with better resolution. Losses due to reflection at the interface seen in Fig. 4(b) render a more negative effect on the quality of the image than stronger dissipative losses existing in the system in Fig. 4(a). The impedance matching in the design of a subwavelength hyperlens was achieved in Ref. [18], where image magnification was numerically realized using principles of transformation optics.

The effect of negative refraction at the interface results in the focusing of emitted radiation in the second slab, similarly to image formation in Pendry's lens. Owing to two paths with equal optical length, the local field at the focus is enhanced by constructive interference. An estimate for the characteristic size of the image is limited by the pixel size, ~ 10 nm in Fig. 4. Additional calculations with the pixel size at about 5 nm indicates, that the waist size at the focal point for the image in Fig. 4 does not exceed 10 ± 5 nm, i.e., it lies in a deeply subwavelength range.

It is clearly seen in Fig. 4 that electromagnetic energy radiated by the dipole is concentrated asymptotically within two narrow cones along the lines separating the regions with metallic and dielectric response. Although the interface is in the near zone, the tendency for concentration of energy along these lines is already clearly seen. Radiation of a dipole in an uniaxial dielectric medium was calculated in Ref. [19]. Detailed distribution of the field pattern in a homogeneous hyperbolic medium was studied in Ref. [20]. Distribution of light intensity in each half-plane in Fig. 4 coincides qualitatively with that obtained in Ref. [20] for a dipole oriented perpendicular to the optical axis.

IV. EFFECTIVE PARAMETERS OF LAYERED AND WIRED STRUCTURES

Homogeneous media a with $\varepsilon_{\perp}^a < 0$, $\varepsilon_{\parallel}^a > 0$ and b with $\varepsilon_{\perp}^b > 0$, $\varepsilon_{\parallel}^b < 0$ can be considered as long-wavelength limits of periodic layered and wired structure, respectively. Their dielectric properties in the homogenization limit can be calculated analytically. The selected layered structure

consists of layers of silver with dielectric function $\varepsilon_m(\lambda)$ and thickness p separated by layers of silicon oxide with parameters ε_d and q . In the long-wavelength limit, $d = p + q \ll \lambda$, where λ is the wavelength in vacuum, the effective dielectric function $\varepsilon_{\parallel}^a(\lambda)$ corresponding to plasmonic-like mode is obtained from the equation [21]

$$\begin{aligned} & \cos \left(\frac{2\pi p}{\lambda} \sqrt{\frac{\varepsilon_m}{\varepsilon_{\parallel}^a} - 1} \right) \cos \left(\frac{2\pi q}{\lambda} \sqrt{\frac{\varepsilon_d}{\varepsilon_{\parallel}^a} - 1} \right) \\ & - \frac{1}{2} \left(\frac{\varepsilon_d}{\varepsilon_m} \sqrt{\frac{\varepsilon_m - \varepsilon_{\parallel}^a}{\varepsilon_d - \varepsilon_{\parallel}^a}} + \frac{\varepsilon_m}{\varepsilon_d} \sqrt{\frac{\varepsilon_d - \varepsilon_{\parallel}^a}{\varepsilon_m - \varepsilon_{\parallel}^a}} \right) \\ & \sin \left(\frac{2\pi p}{\lambda} \sqrt{\frac{\varepsilon_m}{\varepsilon_{\parallel}^a} - 1} \right) \sin \left(\frac{2\pi q}{\lambda} \sqrt{\frac{\varepsilon_d}{\varepsilon_{\parallel}^a} - 1} \right) = 1. \end{aligned} \quad (10)$$

The effective dielectric function $\varepsilon_{\perp}^a(\lambda)$ is explicitly given by the following formula [21]:

$$\begin{aligned} \varepsilon_{\perp}^a(\lambda) = & \frac{\lambda^2}{2(\pi d)^2} \left[1 - \cos \left(\frac{2\pi p}{\lambda} \sqrt{\varepsilon_m} \right) \cos \left(\frac{2\pi q}{\lambda} \sqrt{\varepsilon_d} \right) \right. \\ & + \frac{1}{2} \left(\sqrt{\frac{\varepsilon_m}{\varepsilon_d}} + \sqrt{\frac{\varepsilon_d}{\varepsilon_m}} \right) \sin \left(\frac{2\pi p}{\lambda} \sqrt{\varepsilon_m} \right) \\ & \times \left. \sin \left(\frac{2\pi q}{\lambda} \sqrt{\varepsilon_d} \right) \right]. \end{aligned} \quad (11)$$

The wired structure of period d consists of silver cylinders of radius R imbedded in a silicon dioxide background. The effective dielectric function $\varepsilon_{\parallel}^b$ is the weighted average of ε_m and ε_d

$$\varepsilon_{\parallel}^b = f \varepsilon_m + (1 - f) \varepsilon_d, \quad (12)$$

where $f = \pi R^2 / d^2$ is the filling fraction of metal. The other effective dielectric function is expressed through a series over the reciprocal lattice vectors \mathbf{G} [22],

$$\varepsilon_{\perp}^b = \left\{ \bar{\eta} - \frac{1}{2} \sum_{\mathbf{G}, \mathbf{G}' \neq 0} \mathbf{G} \cdot \mathbf{G}' \eta(\mathbf{G}) \eta(-\mathbf{G}') M^{-1}(\mathbf{G}, \mathbf{G}') \right\}^{-1}. \quad (13)$$

Here $\bar{\eta} = f / \varepsilon_m + (1 - f) / \varepsilon_d$ and

$$\eta(\mathbf{G}) = \frac{1}{A_c} \int_{A_c} \varepsilon^{-1}(\mathbf{r}) \exp(-i\mathbf{G} \cdot \mathbf{r}) d\mathbf{r} \quad (14)$$

is the Fourier component of periodic function $1/\varepsilon(\mathbf{r})$, integration runs over the unit cell with area $A_c = d^2$, and $M^{-1}(\mathbf{G}, \mathbf{G}')$ is the inverse of the matrix

$$M(\mathbf{G}, \mathbf{G}') = \mathbf{G} \cdot \mathbf{G}' \eta(\mathbf{G}' - \mathbf{G}). \quad (15)$$

Using Eqs. (10)–(15) the parameters of any layered or wired nanostructure can be easily calculated. It takes

some effort to optimize the parameters of both structures to satisfy Eq. (9). The following values for the effective dielectric constants were found for the wavelength $\lambda = 670$ nm:

$$\varepsilon_{\perp}^a = -7.05 + i0.18, \quad \varepsilon_{\parallel}^a = 3.90, \quad (16)$$

$$\varepsilon_{\perp}^b = 7.05 + i0.26, \quad \varepsilon_{\parallel}^b = -3.89 + i0.18. \quad (17)$$

These values are obtained for $p = 4$ nm, $q = 6$ nm ($f = p/(p+q) = 0.4$), $R = 5$ nm, $d = 16.45$ nm ($f = \pi R^2/d^2 = 0.29$). The dielectric properties of the constituents at $\lambda = 670$ nm were collected from Ref. [23]: $\varepsilon_{Ag} = -20.86 + i0.43$, $\varepsilon_{SiO_2} = 2.18$, $\varepsilon_{Al_2O_3} = 3.07 + i0.07$. Note that the value of $\varepsilon_{\parallel}^a$ is pure real because the corresponding imaginary part does not exceed 10^{-2} and can be neglected.

For both structures, the ratio $d/\lambda \sim 10^{-2}$ corresponds to a deeply subwavelength limit. Therefore, the obtained values of the effective dielectric constants are quite close to that obtained in the quasi-static limit or in the Maxwell-Garnet approximation.

V. SUBWAVELENGTH IMAGING WITH LAYERED AND WIRED STRUCTURES

We propose a finite size realistic imaging system with the materials and geometrical parameters mentioned previously. Medium *a* (upper slab) contains seven periods of Ag/SiO₂ bilayer with an extra layer of SiO₂ on the top. Medium *b* is a slab of photonic crystal of vertical Ag nanowires in Al₂O₃ matrix of total thickness approximately 240 nm. The distribution of light emitted by a dipole in this structure is shown in Fig. 6.

It is clear from Fig. 6 that the general pattern of light distribution is similar to that obtained for the uniform slabs in Fig. 4. Namely, light emitted by the dipole propagates within a narrow cone, along the straight lines making angles $\pm\varphi(\theta_{min})$ with axis *x*. After negative refraction at the interface, two waves interfere at the focal point. However, one can emphasize some features specific for the structured slabs in Fig. 6. In the multilayer slab, each beam extends along the metal-dielectric boundaries due to surface plasmon-polariton excitation. Similarly, the beams extend along the wires in the second slab, where bright areas appear in the space between the wires, and darker areas are the metallic wires. Owing to beam extension in two orthogonal directions in the wired and layered medium, the symmetry between the source of light and its image, which is obvious from Fig. 4, is lost. Note that the metallic inclusions are practically transparent for light because the optical skin depth $c/\omega_p \approx 22$ nm exceeds their thickness. Here $\omega_p = 8.9$ eV is the plasma frequency for silver. Owing to the inequality $c/\omega_p \ll R$, the magnetization of silver wires in the ac field emitted by the dipole can

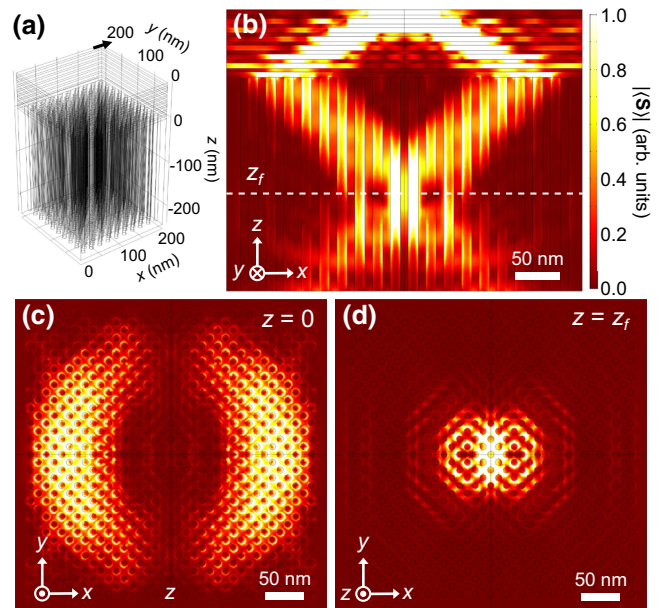


FIG. 6. (a) Proposed scheme of the imaging system with layered and wired structures. The black arrow at the top corner is a dipole radiating at $\lambda = 670$ nm; (b) distribution of averaged Poynting vector $|\langle S \rangle|$ in the *x*-*z* plane where the dipole is displaced (at $y = 200$ nm); (c),(d) distribution of $|\langle S \rangle|$ in the *x*-*y* cross-section at the interface $z = 0$ and at the focal plane $z = z_f$, respectively.

be neglected [24]. Distribution of intensity in Fig. 6 supports interpretation of HMMs as a medium that supports propagation of coupled surface plasmon modes [25].

Figure 6(c) demonstrates the spatial distribution of light intensity in the interface plane $z = 0$. The maximum intensity is observed in the plane of polarization of propagating TM wave (*x*-*y* plane) within the base of the resonance cone. The intensity is minimal along axis *z*, where the evanescent TE wave is polarized. The distribution of intensity in the focal plane $z = z_f$ is shown in Fig. 6(d). The position of the focal plane is obtained as a half height on the curve of intensity distribution over *z*. A wired structure with higher intensity in the dielectric background can be clearly seen in Figs. 6(c) and 6(d). To estimate the size of the image we used a standard procedure. The image size *l* is calculated as the full width of intensity distribution in the *x*-*y* plane taken at half maximum. It gives $l_x \approx 35$ nm along axis *x* and $l_y \approx 50$ nm along axis *y*. These subwavelength values exceed the resolutions reported in previous studies performed at shorter wavelengths. For example, for the image shown in Fig. 6(d) the ratio $l/\lambda = 0.075$. The results reported in Refs. [10,11,26] for l/λ are 0.41, 0.37, and 0.55, respectively. At the same time, much higher image resolution, $\lambda/117$, was obtained in the microwave region [27]. In the microwave experiment with Weyl metacrystal the obtained resolution of 0.2 was relatively low [7].

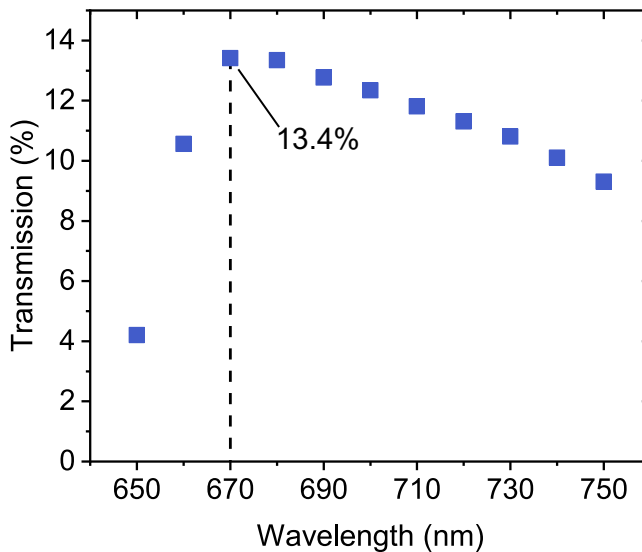


FIG. 7. Transmission of emitted light versus wavelength.

The efficiency of the proposed imaging system depends on the wavelength. The main factor is the transmission ratio T , which is the ratio of intensities at the focus and near the source. The plot of transmission ratio for the wavelength interval 650–750 nm is shown in Fig. 7. Appropriate choice of the filling factor of silver in both hyperbolic media makes it possible that each point in the graph fulfilled the matching conditions Eq. (9). The maximum at 670 nm is because of competition between the resonant enhancement of electromagnetic field in a collection of metallic nanoparticles [28] and Joule dissipation. Both these factors vary with the wavelength that leads to the maximum of transmission at $\lambda = 670$ nm. Higher than 10% transmission is predicted for the bandwidth 660–740 nm.

The proposed scheme needs a combination of layered and wired hyperbolic media to produce a focused image of an object in the near field. The optical hyperlens proposed in Ref. [8] and experimentally realized in Ref. [10] transfers subwavelength pattern in the far field using hyperbolic medium with cylindrical symmetry without focusing. Owing to curved geometry the hyperlens magnifies the image, whereas the image clarity deteriorates. In the spherical hyperlens realized in Ref. [11], the subdiffractive image is formed by narrow weakly divergent beams. Almost nonspread propagation is realized because of flattened isofrequency contours with relatively large curvature. This spherical hyperlens produces subwavelength image in two lateral dimensions. A flat lens with $n \approx -1$ has been fabricated in Ref. [26]. It produces high-quality images with subwavelength resolution in the ultraviolet.

The lenses proposed in Refs. [8,10,26] allow subwavelength patterning beyond the near field. Our scheme produces image at the near-field with higher resolution. For

the image in Fig. 6(d) the resolution $l/\lambda = 0.075$ far exceeds the results $l/\lambda = 0.41, 0.37$, and 0.55 reported in Refs. [10,11,26], respectively. Higher resolution is achieved because of presence of two hyperbolic media, that guarantees preservation of the subwavelength components up to the focal point. The proposed near-field scheme is valid for subwavelength photolithography [12].

A possibility of imaging using two hyperbolic media was proposed by Zhao *et al.* [29]. The imaging system proposed there consists of two layered structures with the same metallic (silver) and different dielectric (air and high refractive index polymer) constituents. An ultraviolet image of an object of two subwavelength slits was obtained by numerical modeling. Our scheme is also based on two metamaterials similar to that in Ref. [29]. However, in our case a combination of layered and wired structures allows conjugate hyperbolic media to be naturally achieved with different signs for ϵ_{\parallel}^a and ϵ_{\parallel}^b as well as different signs for ϵ_{\perp}^a and ϵ_{\perp}^b . In our scheme, the conditions of perfect transmission through the interface (9) can be easily satisfied. For two-layered media with the same metal, these conditions cannot be fulfilled at reasonable filling fractions of metal leading to essential losses at reflection.

VI. CONCLUSIONS

We proposed an optical near-field imaging system with deeply subwavelength resolution based on interfaced type I and type II hyperbolic media. The subwavelength image of a point source is formed by two interfering beams propagating along symmetric optical paths separating the regions with metallic and dielectric response. The hyperbolic media with the necessary optical parameters can be realized as metal-dielectric composites with layered and wired structures operating in the regime of homogenization. Light radiated by a source in the layered medium suffers from negative refraction at the interface and is focused at the symmetric point in the wired medium. The proposed imaging system produces an image of about 50 nm wide of a point dipole radiating at the wavelength of 670 nm. The proposed imaging scheme may be applied for construction of flat hyperlenses with subwavelength resolution and other devices of subwavelength optics.

ACKNOWLEDGMENTS

This work has been partially supported by CONACyT (Mexico) through Grant No. A1-S-23120 and by the NSF (EFRI Grant No. 1741677). K.B. is supported by the State budget of the Russian Federation (IA&E SB RAS Grant No. 121030500067-5).

APPENDIX

Let a plane wave with TM polarization and amplitude E_0 be incident on an interface between two uniaxial optical

crystals. Orientation of the vectors \mathbf{k} , \mathbf{E} , and $\mathbf{S} \parallel \mathbf{v}_g$ in the incident and refracted wave is clear from Figs. 2 and 3(a). Magnetic field H is parallel to axis y and tangential component of electric field $E_x = (ck_z/\omega\epsilon_{\perp})H$. Continuity of the magnetic field H and electric field E_x at the interface $z = 0$ leads to the set of linear equations

$$\begin{cases} H_i + H_r = H_t \\ \frac{1}{\epsilon_{\perp}^a} (k_{(i)z} H_i + k_{(r)z} H_r) = \frac{k_{(t)z}}{\epsilon_{\perp}^b} H_t. \end{cases} \quad (\text{A1})$$

Here indices i , r , and t label the components of the incident, reflected, and transmitted wave, respectively. Solving these equations with respect to H_r and H_t we obtain the following Fresnel formulas:

$$H_r = \frac{\epsilon_{\perp}^b k_{(i)z} - \epsilon_{\perp}^a k_{(t)z}}{\epsilon_{\perp}^a k_{(t)z} - \epsilon_{\perp}^b k_{(r)z}} H_i, \quad H_t = \frac{\epsilon_{\perp}^b (k_{(i)z} - k_{(r)z})}{\epsilon_{\perp}^a k_{(t)z} - \epsilon_{\perp}^b k_{(r)z}} H_i. \quad (\text{A2})$$

The x -component of the wave vector is conserved at reflection and refraction

$$k_{(i)x} = k_{(r)x} = k_{(t)x} = \frac{\omega}{c} \sqrt{\epsilon^a(\theta)} \sin \theta. \quad (\text{A3})$$

Here $\epsilon(\theta)$ is defined by Eq. (4) with $\epsilon_{\perp} = \epsilon_{\perp}^a$ and $\epsilon_{\parallel} = \epsilon_{\parallel}^a$. The z -components of the wave vector in the incident and reflected wave are equal by modulus but have opposite signs

$$k_{(i)z} = -k_{(r)z} = \frac{\omega}{c} \sqrt{\epsilon^a(\theta)} \cos \theta \quad (\text{A4})$$

The z -component of \mathbf{k}_t in the transmitted wave is obtained from the dispersion relation (2). It follows from Fig. 2 that $\operatorname{Re} k_{(t)z} < 0$, i.e.,

$$k_{(t)z} = -\frac{\omega}{c} \sqrt{\epsilon_{\perp}^b \left(1 - \frac{\epsilon^a(\theta)}{\epsilon_{\parallel}^b} \sin^2 \theta \right)}. \quad (\text{A5})$$

The reflection coefficient is defined as

$$R = \frac{|H_r|^2}{|H_i|^2} = \left| \frac{\epsilon_{\perp}^a k_{(t)z} - \epsilon_{\perp}^b k_{(i)z}}{\epsilon_{\perp}^a k_{(t)z} + \epsilon_{\perp}^b k_{(i)z}} \right|^2, \quad (\text{A6})$$

where the components of the wave vectors are given by Eqs. (A4) and (A5).

If both media are dissipationless the reflection coefficient is equal to 1 at $\theta = \theta_c$. The critical angle θ_c , which is the angle of total internal reflection, is obtained from the condition of vanishing $k_{(t)z}$, i.e., vanishing of the transmitted wave. It is clear that $R = 1$ if $k_{(t)z} = 0$ in Eq. (A6). Moreover, for conjugate media (9) this remains true even for $\theta < \theta_c$ because the components $k_{(i)z}$, $k_{(r)z}$, and $k_{(t)z}$

become pure imaginary and the phase of each square root in Eqs. (A4) and (A5) is obtained from the condition of exponential decay of the corresponding evanescent wave. To avoid singularity 0/0 in calculation of the reflection coefficient, the dielectric functions should be taken with infinitesimally small imaginary parts.

-
- [1] V. Veselago, The electrodynamics of substances with simultaneously negative values of ϵ and μ , *Sov. Phys. Usp.* **10**, 509 (1968).
 - [2] J. B. Pendry, Negative Refraction Makes a Perfect Lens, *Phys. Rev. Lett.* **85**, 3966 (2000).
 - [3] R. E. Colin, Frequency dispersion limits resolution in Veselago lens, *Prog. Electromag. Res. B* **19**, 233 (2010).
 - [4] N. Fang, H. Lee, C. Sun, and X. Zhang, Sub-diffraction-limited optical imaging with a silver superlens, *Science* **308**, 534 (2005).
 - [5] D. O. S. Melville and R. J. Blaikie, Super-resolution imaging through a planar silver layer, *Opt. Express* **13**, 2127 (2005).
 - [6] T. Taubner, D. Korobkin, Y. Urzhumov, G. Shvets, and R. Hillenbrand, Near-field microscopy through a SiC superlens, *Science* **313**, 1595 (2006).
 - [7] Ya. Yang, Ya. Bi, L. Peng, B. Yang, Sh. Ma, H.-Ch. Chan, Yu. Xiang, and Sh. Zhang, Veselago lensing with weyl metamaterials, *Optica* **8**, 249 (2021).
 - [8] Z. Jacob, L. Alekseyev, and E. Narimanov, Optical hyperlens: Far-field imaging beyond the diffraction limit, *Opt. Express* **14**, 8247 (2005).
 - [9] A. Salandrino and N. Engheta, Far-field subdiffraction optical microscopy using metamaterial crystals: Theory and simulations, *Phys. Rev. B* **74**, 075103 (2006).
 - [10] Z. Liu, H. Lee, Y. Xiong, Ch. Sun, and Xi. Zhang, Far-field optical hyperlens magnifying sub-diffraction-limited objects, *Science* **315**, 1686 (2007).
 - [11] J. Rho, Z. Ye, Y. Xiong, X. Yin, Z. Liu, H. Choi, G. Bartal, and X. Zhang, Spherical hyperlens for two-dimensional sub-diffractive imaging at visible frequencies, *Nat. Comm.* **1**, 143 (2010).
 - [12] S. Ishii, A. V. Kildishev, E. Narimanov, V. M. Shalaev, and V. P. Drachev, Sub-wavelength interference pattern from volume plasmon polaritons in a hyperbolic medium, *Laser Photonics Rev.* **7**, 265 (2013).
 - [13] J. Yao, Z. Liu, Y. Liu, Y. Wang, C. Sun, G. Bartal, A. M. Stacy, and X. Zhang, Optical negative refraction in bulk metamaterials of nanowires, *Science* **321**, 930 (2006).
 - [14] T. Paul, C. Rockstuhl, C. Menzel, and F. Lederer, Anomalous refraction, diffraction, and imaging in metamaterials, *Phys. Rev. B* **79**, 115430 (2009).
 - [15] L. D. Landau, E. M. Lifshitz, and L. P. Pitaevskii, *Electrodynamics of Continuous Media* (Pergamon Press, New York, 1984), 2nd ed.
 - [16] V. P. Drachev, V. A. Podolskiy, and A. V. Kildishev, Hyperbolic metamaterials: New physics behind a classical problem, *Opt. Express* **21**, 15048 (2013).
 - [17] O. Takayama and A. V. Lavrinenko, Optics with hyperbolic materials, *J. Opt. Soc. Am. B* **36**, F38 (2019).

- [18] Alexander V. Kildishev and Evgenii E. Narimanov, Impedance-matched hyperlens, *Optic Lett.* **32**, 3432 (2007).
- [19] A. O. Savchenko and O. Y. Savchenko, Electromagnetic field of a dipole in an anisotropic medium, *Tech. Phys.* **50**, 1366 (2005).
- [20] A. S. Potemkin, A. N. Poddubny, P. A. Belov, and Yu.S. Kivshar, Green function for hyperbolic media, *Phys. Rev. A* **86**, 023848 (2012).
- [21] A. A. Krokhin, J. Arriaga, L. N. Gumen, and V. P. Drachev, High-frequency homogenization for layered hyperbolic metamaterials, *Phys. Rev. B* **93**, 075418 (2016).
- [22] P. Halevi, A. Krokhin, and J. Arriaga, Photonic Crystal Optics and Homogenization of 2D Periodic Composites, *Phys. Rev. Lett.* **82**, 719 (1999) A. A. Krokhin, P. Halevi, and J. Arriaga, Long-wavelength limit (homogenization) for two-dimensional photonic crystals, *Phys. Rev. B* **65**, 115208 (2002).
- [23] P. B. Johnson and R. W. Christy, Optical constants of the noble metals, *Phys. Rev. B* **6**, 4370 (1972), J. Kanungo and J. Schilling, Experimental determination of the principal dielectric functions in silver nanowire metamaterials, *Appl. Phys. Lett.* **97**, 021903 (2010).
- [24] A. A. Krokhin, E. Reyes, and L. Gumen, Low-frequency index of refraction for a two-dimensional metallocdielectric photonic crystal, *Phys. Rev. B* **75**, 045131 (2007).
- [25] T. Li and J. B. Khurgin, Hyperbolic metamaterials: Beyond the effective medium theory, *Optica* **3**, 1388 (2016).
- [26] T. Xu, A. Agrawal, M. Abashin, K. J. Chau, and H. J. Lezec, All-angle negative refraction and active flat lensing of ultraviolet light, *Nature* **497**, 470 (2013).
- [27] Su Xu, Yu. Jiang, H. Xu, J. Wang, S. Lin, H. Chen, and B. Zhang, Realization of deep subwavelength resolution with singular media, *Sci. Rep.* **4**, 5212 (2014).
- [28] D. A. Genov, A. K. Sarychev, V. M. Shalaev, and A. Wei, Resonant field enhancements from metal nanoparticle arrays, *Nano Lett.* **4**, 153 (2004).
- [29] Ya. Zhao, A. A. Nawaz, Sz-Ch. S. Lin, Qi. Hao, B. Kiraly, and T. Ju. Huang, Nanoscale super-resolution imaging via a metal–dielectric metamaterial lens system, *J. Phys. D: Appl. Phys.* **44**, 415101 (2011).